AIAA JOURNAL
Vol. 45, No. 11, November 2007

Benchmarking Particle Image Velocimetry with Laser Doppler Velocimetry for Rotor Wake Measurements

Manikandan Ramasamy* and J. Gordon Leishman†
University of Maryland, College Park, Maryland 20742

DOI: 10.2514/1.28130

An experiment was conducted to identify and measure the sources of uncertainty that are associated with the application of particle image velocimetry to the measurement of the vortical wakes trailing from helicopter rotor blades. Phase-resolved, three-component particle image velocimetry measurements were performed in the wake of a subscale rotor operating in hover, and were compared with high-resolution three-component laser Doppler velocimetry measurements obtained with the same rotor under identical operating conditions. This helped formulate the essential experimental conditions that need to be satisfied for particle image velocimetry to accurately resolve the high-velocity gradient, high streamline curvature flows that are present inside the rotor wake and in the blade tip vortices. Uncertainties associated with the calibration, acquisition, and processing of the particle image velocimetry images were analyzed in detail. It was shown that the optimization of laser pulse separation time is fundamental to reduce the errors associated with acceleration and curvature effects. Similarly, the interrogation window size was shown to play a critical role in determining the velocity gradient bias errors. The correlation between the laser Doppler velocimetry and particle image velocimetry measurements of the tip vortex characteristics, such as core radius and peak swirl velocity, were found to be excellent.

Nomenclature

A	=	acceleration, m/s^2
C_T	=	rotor thrust coefficient, $=T/\pi\rho\Omega^2R^4$
c	=	chord of the rotor blade, m
d_i	=	image distance, m
d_o	=	object distance, m
d_p	=	seed particle size, μm
d_τ	=	particle image size, μm
L_m	=	measurement volume
l	=	length of a velocity vector
M	=	magnification
N	=	number of points used in the estimation of σ
N_b	=	number of blades
R	=	radius of the rotor blade
r	=	nondimensional radial coordinate
r_c	=	core radius of the tip vortex, m
T	=	rotor thrust, N
V	=	absolute three-dimensional velocity, m/s
V_{norm}	=	normalized tip velocity, $=V_{\theta\max}/V_{\text{tip}}$
V_{tip}	=	tip velocity of the rotor blade, $=\Omega R$, m/s
V_θ, V_r, V_{axial}	=	swirl, radial, and axial velocity components of tip vortex, respectively, m/s
X, Y	=	locations in the camera coordinate system
X_P, Y_P	=	projected length of the calibration target as seen by the camera
x, y, z	=	locations in the object/fluid coordinate system
α, β	=	inclination of the calibration target with respect to x and y axes
ΔR	=	absolute displacement, m
ΔS	=	original distance traveled by the seed particle, m
Δt	=	pulse separation time, μs
ΔX, ΔY	=	displacement in the camera coordinate system, pixels
Δx, Δy, Δz	=	displacement in the fluid coordinate system, m
δx, δy, δz	=	uncertainty in the estimation of x, y, and z, m
ϵ	=	absolute error
ϵ_b	=	bias error
λ	=	wavelength of the laser light, nm
v_i	=	induced velocity, m/s
ρ	=	density of air, kg/m^3
σ	=	standard deviation
σ_e	=	rotor solidity, $=N_bc/\pi R$
Ω	=	rotor rotational frequency, Hz

Received 1 October 2006; revision received 14 June 2007; accepted for publication 16 June 2007.

*Assistant Research Scientist, Department of Aerospace Engineering; mani@umd.edu. Member AIAA.

†Minta Martin Professor of Engineering, Department of Aerospace Engineering; leishman@umd.edu. Associate Fellow AIAA.

I. Introduction

DEVELOPING a comprehensive knowledge of the evolutional characteristics of the wakes trailing from helicopter rotor blades is essential for developing strategies aimed at reducing adverse wake-induced effects, such as blade vortex interaction noise, rotor vibration levels, unsteady blade airloads, and rotor wake airframe interactions. A considerable amount of experimental research has been conducted over the last several decades toward this objective [1–6]. These measurements have been made at different facilities, with different rotors at different rotor operating conditions, and using different measurement techniques [1,2,5,7–11]. Therefore, it becomes imperative to understand the measurement uncertainties associated with each type of experiment if the goal is ultimately to understand accurately the rotor flow physics. The analysis of measurement uncertainty is also essential when the various measurements are used for validating computational predictions, which are now reaching unprecedented levels of capability. Furthermore, the application of semi-empirically developed rotor wake and vortex models [9] in comprehensive predictive analyses means that any measurement uncertainty always directly propagates into the rotor loads and performance predictions [12], and this is of continuing concern in attempts to improve helicopter performance.

Different measurement techniques have been employed to understand the formation and evolution of the blade tip vortices and the associated wake structures trailing from helicopter rotor blades. For example, intrusive techniques such as hot wire anemometry (HWA) have been used for measuring the flowfields of both full-scale [1,10] and subscale helicopter rotors [13,14]. The biggest problem encountered in using HWA for rotor wake measurements,

however, is spatial proximity concerns to the rotor blades, which prevents measurements of young, newly created tip vortices. HWA also suffers from directional flow ambiguity. Furthermore, the lower spatial resolution of HWA is known to be insufficient to resolve the high-velocity gradients inside rotor blade tip vortices [12].

The application of optical flow measurement techniques such as laser Doppler velocimetry (LDV) and particle image velocimetry (PIV) has gained much popularity for rotor wake studies because of their nonintrusive nature (except for seeding the flow) in measuring a given flowfield. One-component (1-C), two-component (2-C), and three-component (3-C) LDV measurements have been successfully made [3,15,16]. The biggest advantage of LDV is its high spatial resolution ($\approx$80 μm) when operated in 3-C coincidence mode, which allows the high-velocity gradients inside the vortex cores to be measured very accurately [3]. Higher spatial resolution also means that the minimum measurable flow structure length scale is smaller. However, LDV is a point-by-point measurement technique that requires a substantial amount of time to map out a given flowfield, especially inside a rotor wake. This shortcoming is, however, mostly overcome by the use of PIV, which measures the velocity in a plane at a given instant of time. Several studies have been performed with PIV to understand the process of making accurate flowfield measurements [17–20], but not previously for the rotor wake environment. It is to this end that the present work is directed.

PIV is a nonintrusive experimental technique, which allows the instantaneous 2-C or 3-C measurement of a planar flowfield by imaging the scattered light from small particles in the flow that are illuminated by a laser sheet. The acquired images are divided into small interrogation regions (called interrogation windows), which are statistically analyzed to produce a correlation peak that represents the magnitude of the particle displacement within the interrogation region. Similar displacements that are estimated through all of the interrogated regions enable the development of a velocity vector map over the entire region of interest. Even though (in principle) PIV consumes a much shorter testing time than LDV to resolve a given flowfield, it has suffered from relatively poor spatial resolution compared to LDV. This has limited its application to rotor wake flows in general, and for vortex flow measurements in particular [21]. The importance of spatial resolution was demonstrated by Martin et al. [12]. It was shown that a measurement technique that had poor spatial resolution [22] yielded a nonphysical result, whereas that with good spatial resolution yielded sufficiently accurate measurements [3]. Thanks to the recent improvements in optics and electronics, higher resolution digital cameras can now give spatial resolutions in the flow comparable to those of 3-C LDV, and can be employed for successfully making measurements inside a rotor wake.

However, understanding the uncertainties associated with any measurement technique is critical for interpreting the measurements accurately. Even though LDV and PIV are nonintrusive to the flowfield (except for the seed particles), both techniques contain various similar yet different types of measurement uncertainties, which can have substantial effects on the resulting flow measurements. A detailed analysis of the uncertainties in LDV for measuring vortex flows was made by Martin et al. [12]. No similar analysis has yet been undertaken for the application of PIV to the same (or similar) types of flows. Most of the existing PIV literature examines the uncertainty associated with the spatial aperiodicity of the tip vortices, and in developing procedures to correct for it (for example, the conditional averaging corrections of McAlister [4] and Van der Wall et al. [23,24]). This uncertainty is significant while estimating the mean velocity from a sequence of phase-locked instantaneous velocity flowfields. However, no uncertainty analysis has been previously made for measuring the instantaneous velocity vector field. Such an analysis is essential, especially in the high-velocity gradient streamline curvature flows produced in rotor wakes and, in particular, by the rotor blade tip vortices [12].

In the present study, an experiment was conducted to identify and measure the sources of uncertainty associated with the application of 3-C PIV for measuring the flowfield of a helicopter rotor. Such an analysis helps to formulate general criteria that need to be satisfied for the successful application of PIV to rotor wake flows. The PIV measurements were compared with high-resolution 3-C LDV measurements of the same flow.

II. Experimental Setup of Rotor Facility

A single bladed rotor operated in the hovering state was used for all flow measurements. The rotor blade used in the experiment was of rectangular planform, untwisted, with a radius of 406 mm (16 in.) and chord of 44.5 mm (1.752 in.), and was balanced with a counterweight. The blade airfoil section was the NACA 2415 throughout. The rotor tip speed ΩR was 89.28 m/s (292.91 ft/s), giving a blade tip Mach number and tip chord Reynolds number of 0.26 and 272,000, respectively. All the tests were made at an effective blade loading of $C_T/\sigma_e \approx 0.064$ using a collective pitch angle of 4.5 deg (measured from the chord line); the zero-lift angle of the NACA 2415 airfoil is approximately -2 deg at the tip Reynolds number. During these tests, the rotor rotational frequency was set to 35 Hz ($\Omega = 70\pi$ rad/s).

The flow at the rotor was seeded with a thermally produced mineral oil fog. The average size of the seed particles (0.2 to 0.22 μm in diameter) was small enough to minimize the particle tracking errors for the vortex strengths found in these experiments [25]. The fundamental requirement of seed particles to track the flow and their influence on the PIV image processing will be discussed later. The entire test area was uniformly seeded before each sequence of measurements, and the fog density was replenished as needed.

The PIV system included dual pulsed Nd:YAG lasers (with a wavelength of 532 nm and capable of firing up to 15 Hz) that operated in phase synchronization with the rotor, a pair of digital charge-coupled device (CCD) cameras (Powerview Plus cameras with 12-bit resolution) with 2 megapixel resolution placed on the same side of the light sheet, a high-speed digital frame grabber, and analysis software (TSI-InSight3G). The cameras were placed at 20 deg from the midpoint of the region of focus (ROF) and satisfy the Scheimpflug criteria to have uniform focus across the entire region of interest. A schematic of the experimental setup is shown in Fig. 1. The two lasers were fired with 110 mJ energy per pulse, and at a default pulse separation time of 1 μs. This corresponds to less than 0.01 deg of blade motion. Over 100 images were captured at each wake age and were phase averaged to estimate the mean flow velocities.

III. Principle of Operation

The PIV technique measures the instantaneous velocity in the flowfield based on the expression

$$V = \frac{M\Delta R}{\Delta t} \tag{1}$$

where ΔR is the displacement of the seed particles over a given pulse separation time Δt, and M is the image magnification given by

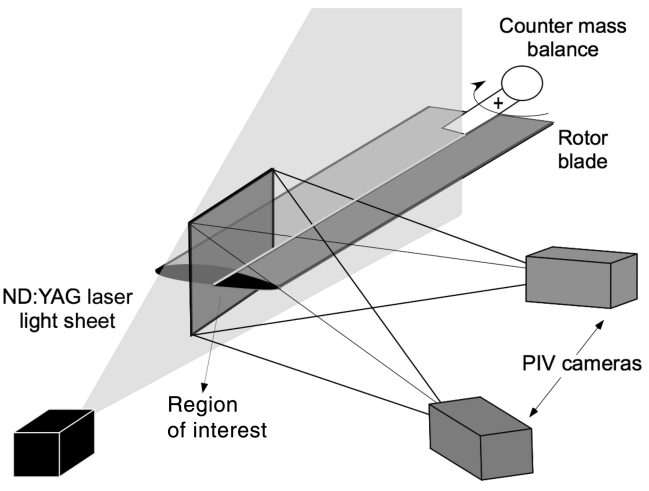

Fig. 1 Schematic of the current experimental setup.

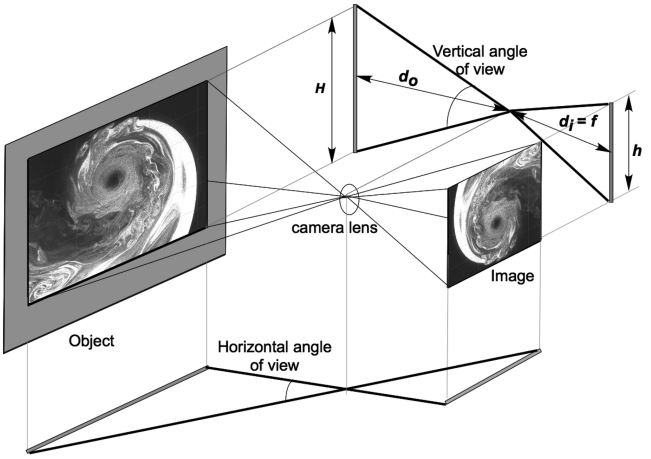

Fig. 2 Schematic explaining the field of view of the camera optics.

$$M = \frac{h}{H} = \frac{d_i}{d_o} \tag{2}$$

Here, h and H are the image and the object size, respectively. The magnification can also be defined as the ratio of the image distance d_i to the object distance d_o as shown in Fig. 2. In the case of a digital CCD camera, this is the ratio of the sensor size to the object size. Equation (1) shows the fundamental steps involved in performing PIV measurements in any given flowfield: 1) calibration for estimating the magnification involved in the process; 2) image acquisition for estimating the displacement of seed particles in the region of focus of the flow; and 3) image processing to calculate the flow velocity.

In the present study, the stereo calibration for 3-C flowfield measurements was performed using a dual plane, double-sided calibration target that is black in the background with white markers —see Fig. 3. The target has two planes of marker points such that the alternate markers are in different planes. The planes are separated by 1 mm. The target is placed in such a way that the two marker planes are on either side of the laser light sheet. A fiducial point in the center acts as the reference or origin of the PIV coordinate system. The location of this point is an input, and the other coordinates are computed relative to this fiducial mark. The two plane target setup allows the computation of the calibration coefficients without traversing the target in the out-of-plane direction. However, as a result, the measured out-of-plane velocity component is only first order accurate. A detailed discussion on the calibration procedure employed in the present study is given in [26].

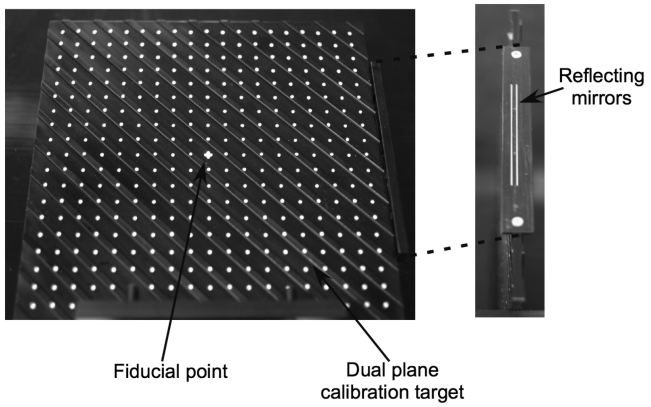

Fig. 3 Calibration target used in the experiment, with side mirror.

IV. Processing Procedure

The acquired image pairs were subdivided into smaller interrogation windows for analysis. Each interrogation window produces one independent 3-C displacement vector. These interrogation windows between the image pairs are cross correlated using a defined algorithm, such as direct correlation or the fast Fourier transform (FFT) correlation. Once the correlation is complete, the correlation peak is estimated (for subpixel displacements) based on curve fitting the correlation signal. Various methods such as bilinear curve fit, three-point Gaussian, or parabolic fit and centroid estimation may be used for estimating the correlation peak.

A simple correlation algorithm uses interrogation windows in both the reference and displaced images of the same size and with no offset, that is, both the windows are placed at the same place in the fluid. For a typical displacement, as shown in Fig. 4a(i), it can be seen that this procedure (single iteration) results in a loss of particle image pairs; only four particle images are used for estimating the correlation signal. Such a low number of contributing pairs may result in incorrect estimates of particle displacement, and hence errors in the measured flow velocity. This can, however, be improved by offsetting the second window (dotted line) based on the displacement estimated from the first iteration. This window offsetting process improves the number of particle images that contribute to the estimation of the correlation peak—see Fig. 4a(ii). Another alternate means to improve the number of contributing particle image pairs is to have the second window larger than the first window, as shown in Fig. 4a(iii).

For flowfields with very high-velocity gradients such as found inside a helicopter rotor wake, a new and improved recursive technique called the iterative deformation grid correlation has been

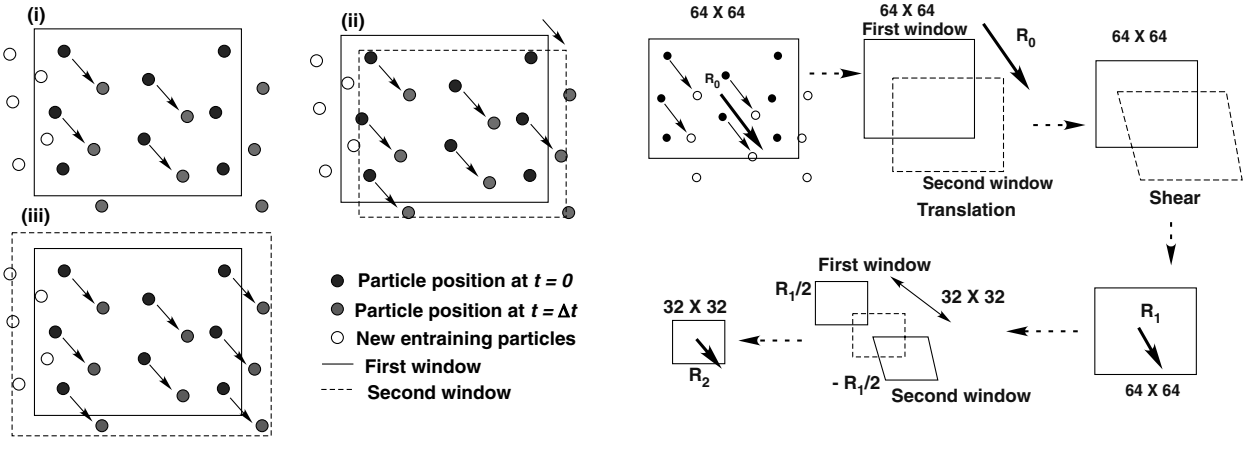

a) Correlation choices **b) Iterative deformation grid**

Fig. 4 Schematic explaining a) the choices of the correlation procedure, and b) the sequence of steps followed in the iterative deformation grid correlation used in the present study.

developed by Scarano [27]. Here, the procedure involves both shear and translation of interrogation windows instead of just the simple translation—see Fig. 4b. The procedure starts with the correlation of an interrogation window of a defined size (say, 64×64), which is the first iteration. Once the mean displacement of that region is estimated, the interrogation window of the displaced image is moved by integer pixel values for better correlation in the second iteration. This third iteration starts by moving the interrogation window of the displaced image by subpixel values based on the displacement estimated from the second iteration. Following this, the interrogation window is sheared twice (for integer and subpixel values) based on the velocity magnitudes from the neighboring nodes, before performing the fourth and fifth iterations, respectively.

Once the velocity is estimated after these five iterations, the window is split into four equal windows (of size 32×32). These windows are moved by the average displacement estimated from the final iteration (using a window size of 64×64) before starting the first iteration at this resolution. This procedure can be continued until the resolution required to resolve the flowfield is reached. The second interrogation window is deformed until the particles remain at the same location after the correlation. This technique, especially the introduction of shear, has been shown in the present work to be very efficient for measuring the high-velocity gradients inside rotor wake flows. For a flow with very high-velocity gradients, however, the average displacement estimated by the largest window (which are used to move the smaller windows) may not be optimum for the smaller windows. This means that the smaller windows may have to be moved by a larger or smaller distance than is required for optimum correlation. This can result in a loss of image pairs. A judicious choice of the initial window size, however, can solve this problem.

In the current study, the recursive deformation grid correlation technique has been used to estimate the flow velocities inside the high-velocity gradient tip vortex cores. Various preconditioning steps may be used to improve the correlation. The average background noise, estimated from all the acquired images, was removed before the correlation. An FFT correlation with a three-point Gaussian fit has been used in this case for the correlation and peak estimation, respectively.

The signal-to-noise ratio (the ratio of the primary peak to the secondary peak of the correlation) was set to 1.5. Even though this is a stringent requirement, such a high value is essential for the accurate estimation of particle displacements. Once the correlation for the entire image was performed, spurious vectors were removed based on the 3σ values and a median tolerance of 2 pixels based on a neighborhood of 5×5 points surrounding each vector. Any spurious vectors were replaced by interpolated vectors from a neighborhood of 3×3 nodes. A 50% overlap has been consistently applied throughout the entire processing area.

V. Measurement Results

The acquired 100 PIV images were processed and simple phase averaged to estimate the mean velocity in the region of focus—see Fig. 5. It should be noted that every eighth vector has been plotted here to prevent image congestion. Because these measurements were made near the blade at a young 3 deg of wake age, the aperiodicity of the tip vortex locations was not significant to require formal correction procedures [3,28]. The figure has vorticity as its background, which clearly shows the presence of a concentrated blade tip vortex. The presence of a turbulent vortex sheet that is trailed from the inner part of the blade can also be identified.

Figure 6a shows the measured tangential, radial, and axial velocity components by making a horizontal cut across the vortex core. By convention, the velocities and the radial distances were normalized by the tip speed of the rotor, and the core radius of the tip vortex, respectively. The core radius was assumed to be half the distance between the two swirl peaks across the center of the vortex. It can be seen that the peak swirl and axial velocity components are 30% and 24% of the blade tip velocity, respectively.

Notice that the peak swirl velocities are not symmetrical on either side of the vortex, mainly because of its nonzero convection velocity

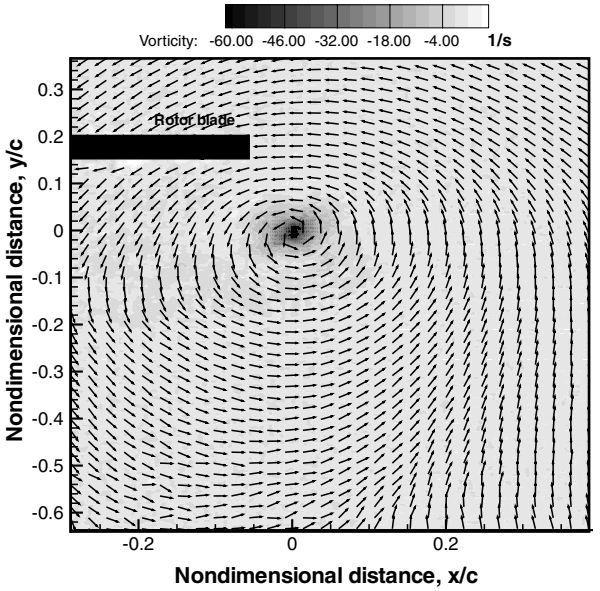

Fig. 5 Flowfield surrounding a tip vortex trailing from a rotor blade at 3 deg wake age (only every eighth vector on either side is plotted to prevent image congestion).

through the flow. The difference between the two peaks on each side of the core can be assumed to be its average convection velocity, which is also a measure of the induced velocity inside the slipstream boundary of the rotor wake. It can be observed that the axial velocity in the vortex has its peak not at the vortex center, but slightly away from its axis; this may be because of the slight inclination of the helical vortex filaments with respect to the measurement plane. It should be noted that there are more than 20 points present inside the vortex core boundary, which is a result of the combination of the reduced region of focus and the higher resolution cameras that were used in the present study.

Figures 6b and 6c show the measured tangential and axial velocities across the tip vortex, along with LDV measurements [3]. Good correlation can be seen between both measurement techniques. In the case of the PIV, every other data point is plotted to prevent image congestion. It can be seen that the peak swirl velocity measured by PIV matches the LDV measurements. Very good agreement can be seen inside the vortex core where the velocity gradients are high. The velocities measured by the two techniques are slightly different outside the vortex core boundary. However, the values are still within the measurement precision.

Similarly, in the case of the axial velocity, the LDV measurements showed lower velocities when compared to the PIV measurements. This may be because of the lower spatial resolution resulting from the on-axis data acquisition technique that was used in LDV instead of the better off-axis mode for axial velocity measurements. This technique reduces the spatial resolution by an order of magnitude (from 3% of the probe volume to 30% relative to the vortex core size). Even in the case of PIV, the probe volume (interrogation window size) is sensitive to the thickness of the laser light sheet.

The measurement of the standard deviation of the normalized swirl velocity across the tip vortex produced by phase averaging is shown in Fig. 6d. It is apparent the standard deviation reaches its maximum value near the vortex core axis. Even though aperiodicity has been previously assumed to be negligible in this case, such variations of standard deviation still suggest the presence of some aperiodicity in the flowfield that spatially alters the phase-resolved tip vortex locations between each PIV acquisition image.

VI. Error Analysis

The difference between the true value of a parameter and its measured value is defined conventionally as the total measurement error, that is,

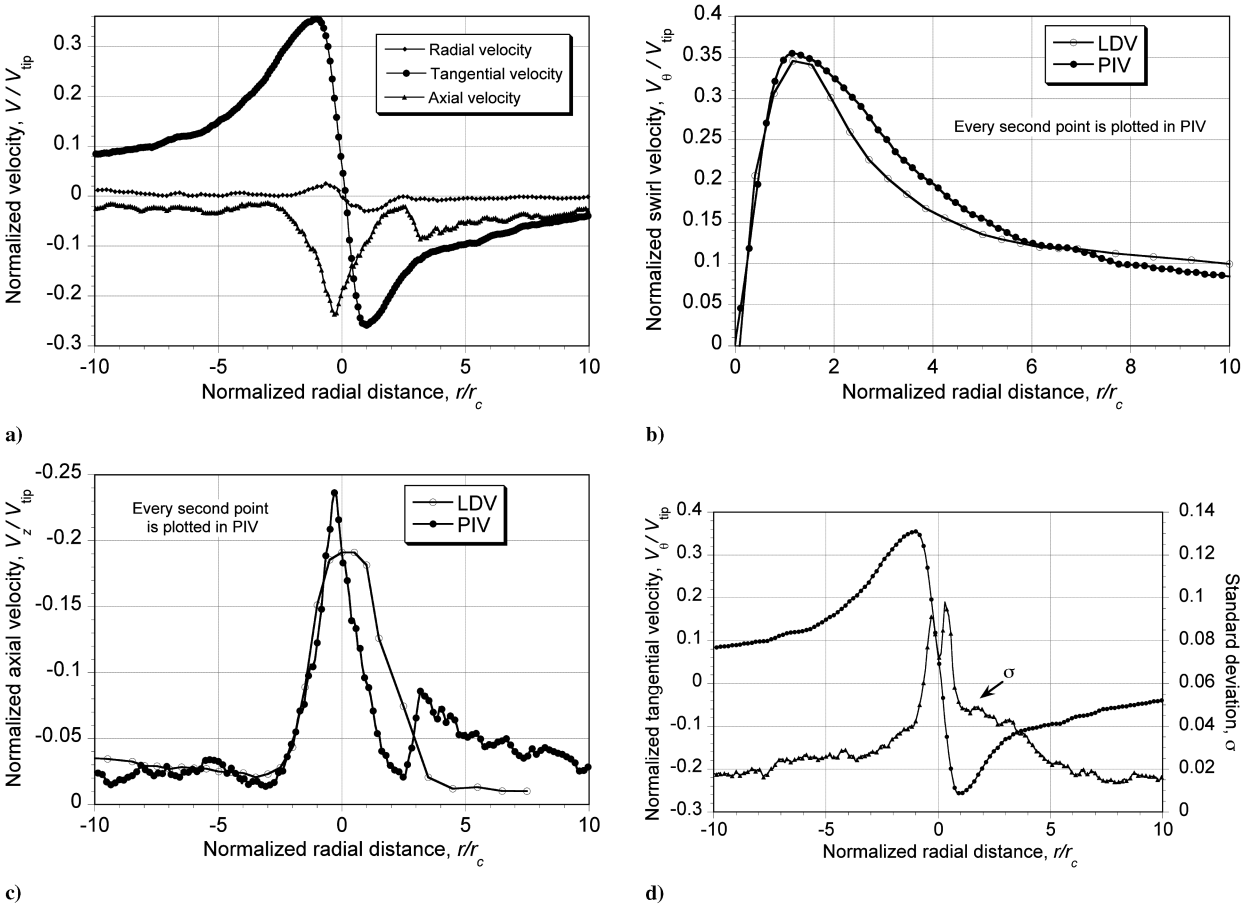

Fig. 6 Various measurements across the tip vortex at $\zeta = 3$ deg: a) normalized velocity components; b) comparison of swirl velocity measured by LDV and PIV; c) comparison of axial velocity measured by LDV and PIV; d) standard deviation of the normalized swirl velocity produced by phase averaging.

$$\epsilon = x_{\text{true}} - x_{\text{measured}} \tag{3}$$

There are two sources for the total measurement error: systematic error and random error. Systematic error is defined as the part of a measurement error that remains constant in repeated measurements of the same true value. Multiple elemental systematic errors, such as the calibration and data acquisition errors, can contribute toward the total systematic error of the flow measurement.

One particular property of this error is that it follows a consistent pattern that can be predicted, which allows for methods to be devised to reduce or, even, remove them. Random error, on the other hand, will vary with repeated measurements of the same true value. The uncertainty associated with the random error can be estimated by inspection of the measurement scatter. The standard deviation σ is generally used to measure the scatter produced by the random error.

VII. Calibration Error

Calibration error has contributions from two sources: 1) the error associated with improper placement of the calibration target, and 2) the error associated with the development of the mapping functions. Even though the error associated with improper placement of the calibration target can be removed in stereoscopic PIV through various techniques [29], the error from the latter source is common to both 2-C and 3-C PIV.

A. Calibration Target

The largest source of calibration error occurs when the calibration target is not placed perfectly to the plane of the laser light sheet. Figure 7a shows the coordinate system of the laser light sheet (x, y, z) along with an improperly placed calibration target of dimension $(X, Y, 1)$ and its projection on the laser light sheet plane. The angles have been exaggerated to give a better understanding of the misalignment. An inclination of α about the x axis (see Fig. 7b) alters the vertical dimensions of the calibration target viewed by the camera. Similarly, an inclination of β in the y axis (see Fig. 7c) alters the horizontal dimensions of the calibration target viewed by the camera. A small displacement along the z axis can alter both the horizontal and vertical dimensions.

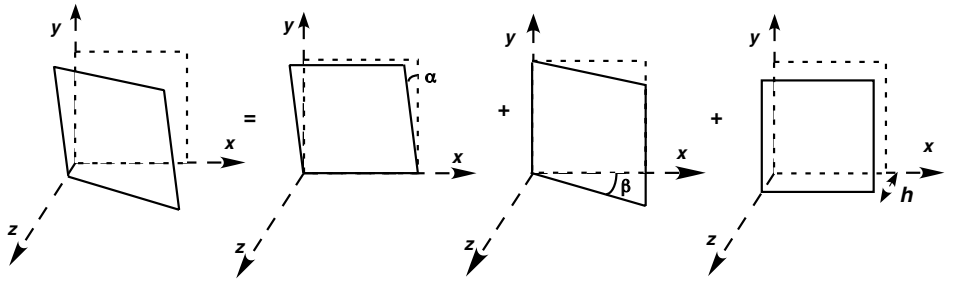

Fig. 7 Schematic showing the possible sources of error in placing the calibration target on the laser light sheet plane.

Here, it should be noted that the horizontal and vertical angles of view of the lens are different—see Fig. 2, which would have a different influence on the magnification along the x and y axes (even though their aspect ratio is maintained constant). Therefore, the uncertainty associated with the estimation of the horizontal and vertical dimensions of the target or their influence on the magnification are given by the equations

$$\delta M_x = \sqrt{\left(\frac{\partial M}{\partial \beta}\right)^2 (\delta\beta)^2 + \left(\frac{\partial M}{\partial z}\right)_x^2 (\delta z)^2} \tag{4}$$

and

$$\delta M_y = \sqrt{\left(\frac{\partial M}{\partial \alpha}\right)^2 (\delta\alpha)^2 + \left(\frac{\partial M}{\partial z}\right)_y^2 (\delta z)^2} \tag{5}$$

Because any vector in the flowfield l can be represented by the x and y coordinates using

$$l = \sqrt{x^2 + y^2} \tag{6}$$

their associated uncertainties can be represented as

$$\delta M = \sqrt{2\delta M_x + 2\delta M_y} \tag{7}$$

In the present study, the calibration target was provided with a mirror along one of its edges. This mirror is used to reflect the laser light sheet back to its source. This significantly reduces the misalignment of the calibration target, however, it does not remove the error completely [29]. This is because the laser light sheet has a finite thickness ($\approx$0.8 mm at its waist in the present study) and it is difficult to detect the alignment of the Gaussian peak of the laser light sheet (source) and the reflected light from the calibration target mirror.

The vertical dimension of the calibration target viewed by the camera from its inclination about the x axis, α, is given by

$$Y_p = Y \cos\alpha \tag{8}$$

where Y_p is the projected length on the laser light sheet as seen by the camera. This would mean that

$$\frac{1}{M}\frac{\partial M}{\partial \alpha} = \sec\alpha \tan\alpha \tag{9}$$

This reduction in the actual distance alters the magnification [based on Eq. (2)] and can, therefore, directly influence the estimation of the flow velocities. Similarly, an inclination in the y axis by β results in

$$X_p = X \cos\beta \tag{10}$$

where X_p is the projected dimension of the calibration target seen by the camera. As a result, then

$$\frac{1}{M}\frac{\partial M}{\partial \beta} = \sec\beta \tan\beta \tag{11}$$

As previously mentioned, compared to the rotation about the x axis (or y axis), a displacement along the z axis will alter the dimensions viewed by the camera in both the x and y axes. In the present study, a 100 mm microlense with F-stop 2.8 was used; this has angles of view of 4.36 and 3.55 deg along the x axis and the y axis, respectively. As a result, the following relationships hold:

$$\frac{1}{M}\left(\frac{\partial M}{\partial z}\right)_x = \frac{2\tan(4.36\ \text{deg})}{X - 2z\tan(4.36\ \text{deg})} \tag{12}$$

and

$$\frac{1}{M}\left(\frac{\partial M}{\partial z}\right)_y = \frac{2\tan(3.55\ \text{deg})}{Y - 2z\tan(3.55\ \text{deg})} \tag{13}$$

Because the estimation of α, β, and z is not possible (other than by knowing their maximum possible values), this would result in $\delta\alpha = \delta\beta = \delta z = 1$. Upon substituting the values of α, β, and z, the total uncertainty in magnification can be estimated using Eq. (7) to be

$$\left(\frac{\delta M}{M}\right) \approx 0.3\%$$

Such a low value is partly because of the use of a convex lens at the end of the optical arm that reduces the thickness of the laser light sheet at the region of focus. The use of a calibration target mirror that helps align the target with the laser light sheet plane also played a significant role in reducing this uncertainty.

This calibration uncertainty can be reduced significantly in the stereoscopic PIV technique. This is done by measuring the calibration target location in the laser light sheet coordinate system using a dewarping process, and cross correlating the flow images. The process is similar to PIV processing, however, the correlating flow images correspond to the same instant in time in this case. If the calibration were to be perfect and the laser light sheet had zero thickness, then the particle images from the same laser pulse (from the two camera images) would be at the same pixel location in both of the dewarped images. A correction based on this principle is given in detail in [29] and has been used in the present study.

B. Mapping Functions

Marker points from the object plane are related to the calibration marker points in the image plane through curve fitting using polynomial equations. However, this curve fitting introduces residual errors that need to be accounted for. In the present study, it was found that the bias error and the standard deviation in identifying a marker point in the image plane to that of the object plane through the developed polynomial equation were 0.0249 and 0.0491 pixels, respectively. A total of 19 points were used for developing the polynomial equation. The total uncertainty would then be

$$\delta X = \sqrt{X_b^2 + P_I^2} \tag{14}$$

where X_b is the bias error and P_I is the precision error that is given by

$$P_I = \frac{t_{95}\sigma}{\sqrt{N}} \tag{15}$$

A student factor of 95% would result in δX as 0.032. This would mean that the uncertainty in identifying a distance in the image plane is $2\delta X$. A distance in the image plane (along X, in the left camera) is generally given by

$$\Delta X_{\text{left}} = \frac{\mathrm{d}X_{\text{left}}}{\mathrm{d}x_{\text{fluid}}}\Delta x_{\text{fluid}} + \frac{\mathrm{d}X_{\text{left}}}{\mathrm{d}y_{\text{fluid}}}\Delta y_{\text{fluid}} + \frac{\mathrm{d}X_{\text{left}}}{\mathrm{d}z_{\text{fluid}}}\Delta z_{\text{fluid}} \tag{16}$$

Assuming that there is no uncertainty in measuring the distance in the calibration target ($\delta x_{\text{fluid}} = \delta y_{\text{fluid}} = \delta z_{\text{fluid}} = 0$), the uncertainty is

$$\begin{aligned} 2\delta X_{\text{left}} = {} & 2\left(\frac{\delta X}{dx_{\text{fluid}}}\right)\Delta x_{\text{fluid}} + \left(\frac{\Delta X}{\Delta x_{\text{fluid}}}\right)\delta\Delta x_{\text{fluid}} \\ & + 2\left(\frac{\delta X}{dy_{\text{fluid}}}\right)\Delta y_{\text{fluid}} + \left(\frac{\Delta X}{\Delta y_{\text{fluid}}}\right)\delta\Delta y_{\text{fluid}} \\ & + 2\left(\frac{\delta X}{dz_{\text{fluid}}}\right)\Delta z_{\text{fluid}} + \left(\frac{\Delta X}{\Delta z_{\text{fluid}}}\right)\delta\Delta z_{\text{fluid}} \end{aligned} \tag{17}$$

Assuming that there is no contribution from y and z on the uncertainty in x, then Eq. (17) can be rewritten as

$$\frac{\delta\Delta x_{\text{fluid}}}{\Delta x_{\text{fluid}}} = \frac{1}{M}\left(\frac{2\delta X_{\text{left}}}{\Delta x_{\text{fluid}}} - \frac{2\delta X}{dx_{\text{fluid}}}\right) \tag{18}$$

It is apparent from this expression that a larger displacement of a particle (Δx_{fluid}) reduces the uncertainty in the estimation of the in-plane particle displacement. This would mean that the uncertainty in

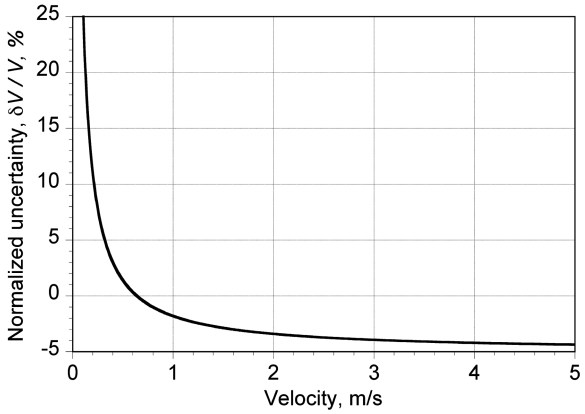

Fig. 8 Normalized measurement uncertainty for varying velocities across the vortex.

the swirl velocity near a vortex core boundary will be smaller because of larger particle displacements for a given pulse separation time than would be found near the vortex core axis.

The out-of-plane displacement is the difference in displacement observed in the image plane of the right and left CCD cameras. This would mean that the uncertainty associated with the out-of-plane component is twice that of the in-plane components, at least theoretically. The velocity is calculated using the expression

$$V = \frac{\Delta x_{\text{fluid}}}{\Delta t} \tag{19}$$

Because the instrument precision for measuring t is 0.05, this would mean that the corresponding uncertainty associated with the estimation of the in-plane velocity is

$$\frac{\delta V}{V} = \frac{\delta \Delta x_{\text{fluid}}}{\Delta x_{\text{fluid}}} - \frac{\delta \Delta t}{\Delta t} \tag{20}$$

This clearly suggests that for the regions where larger particle displacements are observed for a given value of pulse separation time, the biggest source of error will be from the instrument accuracy in setting the pulse separation time.

Figure 8 shows the representative uncertainty associated with the estimation of velocity across the vortex core. Near the vortex axis, it is known that the absolute velocity is substantially smaller than that at the core boundary. As a result, the uncertainty from the estimation of displacement (of particles) is dominant. However, as the velocity increases away from the vortex axis, the displacement uncertainty reduces and asymptotes to the uncertainty resulting from the instrument precision of setting the pulse separation time.

In the present experiments, the measurement bias error across the vortex resulting from the mapping functions is shown in Fig. 9a. Combining the bias error and standard deviation measured across the vortex, the total error is given by

$$\epsilon = \sqrt{\left(\epsilon_b^2 + \frac{t_{95}\sigma}{\sqrt{N}}\right)} \tag{21}$$

where ϵ_b is the bias error, N is the number of samples used to determine the standard deviation σ, and t_{95} is the 95% confidence level in the measurements. The total errors from processing the images for the swirl, radial, and axial velocities are shown in Figs. 9b–9d, respectively. In the case of the swirl velocity, the total error is a maximum near the vortex core axis and then gradually decreases with an increase in radial distance across the vortex. This is consistent with Eq. (18), which suggests that the larger displacement

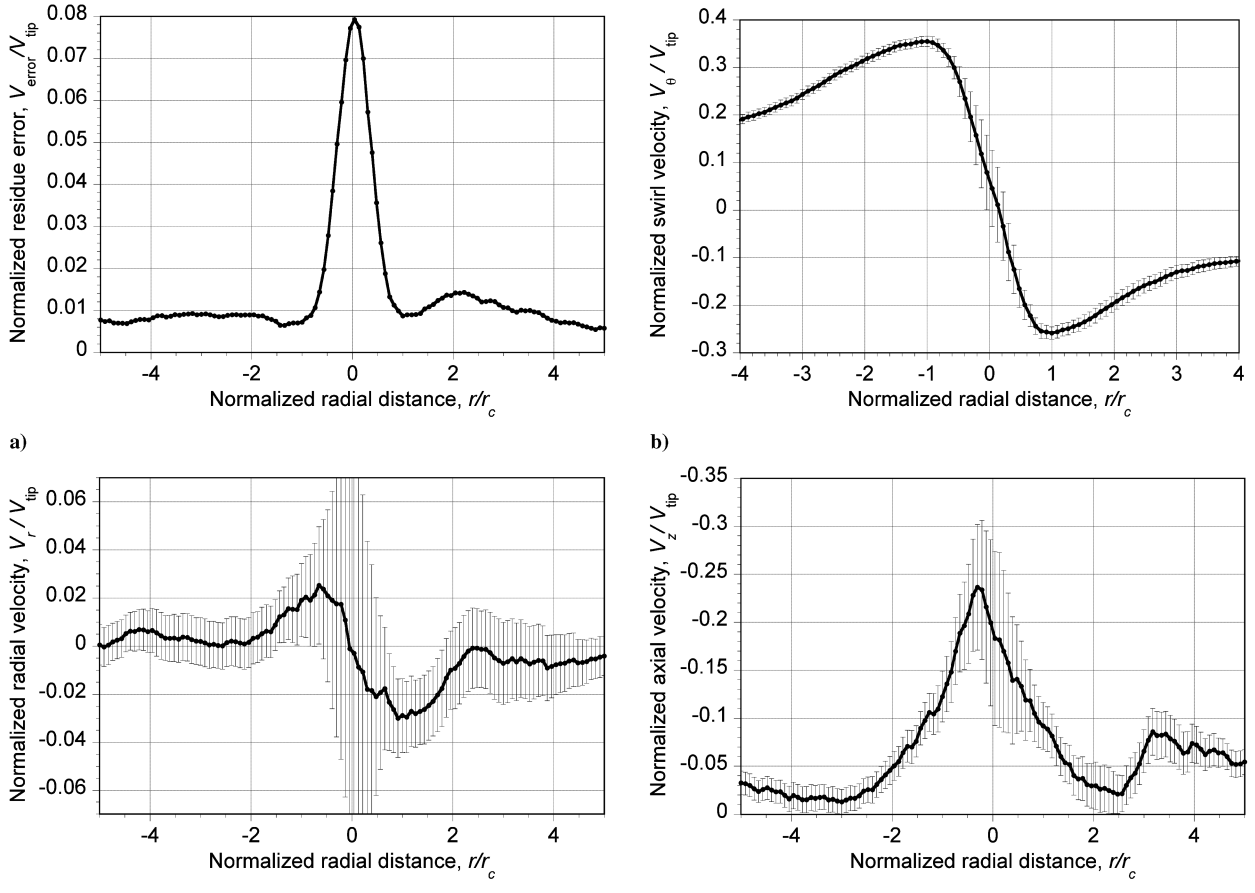

Fig. 9 Variation of different errors across the tip vortex: a) measurement bias error across the tip vortex from the calibrating mapping functions; b)–d) calibration and processing error across the tip vortex for swirl, radial and axial velocity distributions, respectively.

of seed particles (near the core boundary) reduces the uncertainty associated with the measurements.

It can be observed that the axial component exhibits a larger measurement uncertainty than for the tangential velocity. It is known that the axial velocity suffers the most because of aperiodicity issues. This results in a larger scatter in the axial velocity measurements and a larger standard deviation that, in turn, contributes to a higher measurement uncertainty. In the case of the radial velocity, both the bias and precision uncertainties are much larger relative to the magnitude of the normalized radial velocity, even though their absolute value is comparable to those of the tangential and axial velocities.

VIII. Acquisition Uncertainties

The elemental uncertainty associated with data acquisition has multiple sources. These include the bias and random error associated with the size of the seed particles used in the experiment, random errors that result from the noise in the image recording and its subsequent processing, acceleration errors caused by the basic principle of PIV that approximates the Eulerian velocity components based on finite particle displacements, velocity gradient errors that arise because of the difference in velocity across the interrogation window (both random and bias error) [30], and registration errors [31] that result from the imperfect matching of two stereoscopic velocity fields.

Another unique error associated with the PIV technique when measuring vortical rotor wakes and tip vortices is the loss of information about flow curvature. Among these errors, acceleration error and curvature error are dictated by the laser pulse separation time, and the velocity gradient error is caused by the choice of the interrogation window size (spatial resolution).

A. Random Error

The acquired images were first divided into small interrogation windows (generally 32×32 or 64×64). These windows have multiple particle images of size d_τ, which upon correlation yields a signal peak whose diameter is of the order of d_τ. This clearly suggests the need for smaller seed particles. Subpixel displacements can be estimated by various methods that include, but are not limited to, bilinear fit, curve fits such as Gaussian, parabola, etc., or by calculating the centroid. However, this subpixel estimation is influenced by various parameters.

Adrian [32] found that the irregular particle images, imperfections arising from film grain (in the case of film-based PIV), pixel readout noise, nonuniform particle size distribution, and the variation of illumination intensity across the interrogation spot, all contribute toward random error. These errors also scale with the particle image diameter d_τ. Furthermore, the error associated with the random correlation between particles that do not belong to the same image pair, as well as the error associated with the loss of in-plane and out-of-plane image pairs, will contribute to the random error. This random error is given [33,34] by

$$\sigma_{\text{rand}} = c d_\tau \tag{22}$$

where $c = 0.05$–0.07. It is clear from the above expression that the random error reduces with a reduction in the particle image size. Also, a reduction in the particle image size increases the intensity of the reflected light, which can result in improved correlation. However, this may also introduce pixel locking errors, which will be discussed in the next section.

B. Particle Size

The size of the seeding particle plays a substantial role in the experimental errors associated with the measurement of velocity vector fields using the various types of PIV processing algorithms. Seed particles are required to meet certain required criteria, irrespective of the employed measurement technique. Seed particles should be large enough to reflect the incident laser light, which is the primary source of the measurement. However, the particles should be small enough to have low inertial and aerodynamic response time and so will follow the fluid motion without any lag or slip. These contradicting requirements need to be met with a reasonable compromise [25]. From a PIV perspective, there are further requirements to be met for choosing the most suitable size of the seed particles.

The ratio of the particle image diameter and the pixel size of the camera have significant influence on the velocity estimates. The particle image diameter is defined [35,36] as

$$d_\tau = \sqrt{(M d_p)^2 + d_{\text{diff}}^2} \tag{23}$$

where M is the magnification, d_p is the particle size, and d_{diff} is the diffraction limited minimum image diameter. Irrespective of the actual particle size, the image size of the particle seen by the camera is based on diffraction principles. A detailed explanation on this topic is given in [36]. This diffraction limited minimum image diameter is given by

$$d_{\text{diff}} = 2.44 f (M + 1) \lambda \tag{24}$$

where λ is the wavelength of the incident laser light sheet and f is the F-stop of the lense. In the present study, $f = 2.8$ and the laser has a wavelength of 532 nm. An increasing f increases the value of d_{diff}; however, this will also reduce the amount of light entering into the imaging system.

When the particle image size is too small compared with the pixel size (i.e., it is underresolved), this will result in significant bias error because of the finite numerical resolution of the correlation function [34]. The displacement of the particles resulting from this effect will appear to be biased toward an integral pixel value. This effect is called "pixel locking" or "peak locking." The pixel locking effect increases with the reduction in the particle image diameter [37]. A larger value of this ratio increases the random errors that result in pixel readout noise, etc. [32]. This suggests that optimizing the particle image size is essential. An optimum value of 2.1 has been suggested by Prasad et al. [34] based on the random and bias error minimization for a cross-correlation procedure.

In the present study, the ratio of particle image diameter and the pixel diameter was measured to be 0.66. Despite having such a relatively low value for this ratio, the results did not show any peak locking effects—see the histogram shown in Fig. 10. In this case, several factors contribute to the successful elimination of the peak locking effect. These include 1) the increased fill ratio or higher sampling rate, that is, the presence of more particles inside the correlation window (higher density) which result in multiple particles contributing for the peak correlation [29], and 2) improper focusing of the seed particles, which increases the particle image size seen by the camera. Even though preconditioning can also be applied to optimize the particle image diameter with respect to the peak

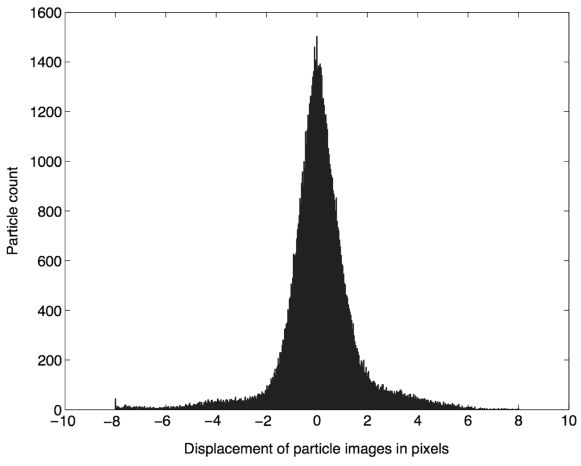

Fig. 10 Typical particle image displacement histogram showing no signs of pixel locking effects.

estimator [36], no such preconditioning has been applied in the present study.

C. Pulse Separation Time

The laser pulse separation time plays a significant role in accurately measuring the instantaneous velocity of a flowfield [38]. This is especially true in the case of rotor blade tip vortices, where significant flow accelerations and flow curvature exists.

The importance of optimizing the pulse separation time can be understood from Fig. 11, which shows the measured tangential (swirl) velocity distribution in a tip vortex for two different pulse separation times, while keeping other variables constant. It is apparent that the swirl velocity profile, peak swirl velocity, and the core radius (three basic defining parameters of a tip vortex) all change with the selected value of Δt. Furthermore, in the case of tip vortices, another unique condition should be satisfied to properly make phase-resolved flow measurements, which is a point previously discussed by Martin et al. [21]. Because the tip vortices in a rotor wake convect at approximately half the average inflow velocity at the plane of the rotor disk, care should be made that the vortex core remains the same position in both the PIV frames. Martin et al. suggested the condition that

$$\Delta t\left(\frac{v_i/c}{c}\right) \leq 0.1\% \tag{25}$$

be met so that the vortex core position lies within 1% of its core size between successive frames. In the present study, care was taken to ensure this condition is satisfied. A Δt value of 1 μs corresponds to less than 0.01%.

D. Acceleration Error

PIV operates on the principle of correlating images that are acquired within a time interval Δt. In the stereoscopic, single plane PIV technique, this means that the location of the particles within the measurement plane at two instants in time $X(t)$ and $X(t + \Delta t)$ is the only stored information used for analysis. Estimating acceleration in a given flowfield requires multiplane PIV measurements [39,40]. Also, because real rotor wake flows can be unsteady (aperiodic) and the flow will always be subjected to accelerations, there will be an error associated with the estimation of velocity based on the particle displacements. For particles that track the fluid without any lag or slip, the trajectory can be approximated [33] as

$$X(t + \Delta t) \approx X(t) + \frac{\mathrm{d}X}{\mathrm{d}t}(\Delta t) + \frac{\mathrm{d}^2X}{\mathrm{d}t^2}\left(\frac{\Delta t^2}{2}\right) \tag{26}$$

This means that the relative error resulting from the acceleration of the flow is given by

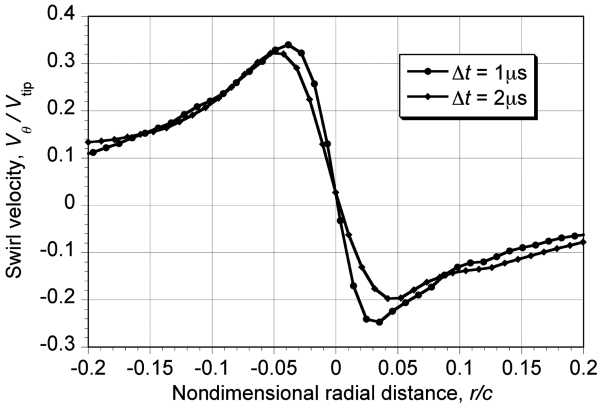

Fig. 11 Swirl velocity distribution in a tip vortex estimated for various laser pulse separation times.

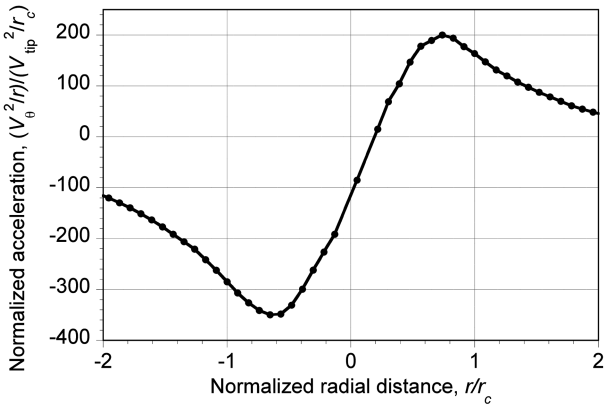

Fig. 12 Centrifugal acceleration across the vortex.

$$\epsilon_{\text{accel}} = \left|\frac{\mathrm{d}v}{\mathrm{d}t}\right|\frac{|\Delta X|}{2Mv^2} \tag{27}$$

where v is the velocity in terms of pixels per second and M is the magnification. It is clear from Eq. (27) that a reduction in pulse separation time, which reduces the particle image displacement, always reduces the error associated with flow acceleration effects.

In the case of tip vortices, centripetal and Coriolis accelerations act on the particles that are distributed across the vortex [25]. The variation of centripetal acceleration across the vortex core (in a 2-component plane) is shown in Fig. 12. For illustration in this case, the acceleration has been estimated based on the expression $A = V_\theta^2/r$. Because the acceleration increases with radial distance, the uncertainty associated with the acceleration increases with radial distance until 75% of the vortex core boundary at $r = r_c$ is reached, at which point the acceleration starts to reduce quickly.

E. Flow Curvature in the Tip Vortices

Another source of error that is significant, and which is lost information in PIV measurements, is flow curvature effects. Because the locations of particles at two instants of time $X(t)$ and $X(t + \Delta t)$ are the only stored pieces of information, the correlation algorithm assumes the smallest distance between the two correlated particle images to be the distance traveled by the particle. Obviously, a significant error can be introduced as a result of this assumption. This is especially true near the vortex core axis, where the flow curvature effects are substantial. This effect can be better understood using the schematic given in Fig. 13. It is apparent that this error always reduces with a reduction in the pulse separation time.

This form of bias error can be reduced by introducing a correction factor obtained using the assumption of an axisymmetric vortex. Based on the estimation of the displacement of particle images measured by PIV and the radial position, it is possible to retrieve this curvature information. From the schematic shown in Fig. 13, it is apparent the original distance traveled by the particle ΔS is different from that assumed by the PIV processing technique. A correction procedure for axisymmetric vortices has been given in [26], which helps retrieve at least some of the lost information on flow curvature.

The foregoing approach helps in estimating the acceptable upper and lower bounds on the laser pulse separation time. It is apparent that the pulse separation time should be as small as possible (i.e., a very small particle displacement) to reduce the errors associated with flow acceleration and curvature effects. However, the displacement of seed particles should be larger than the minimum displacement that can be accurately estimated by the correlation technique.

Recent correlation techniques are capable of estimating the particle displacement within 0.1 pixels. In the present study, the chosen pulse separation time of 1 μs results in an approximately 1 pixel displacement at the vortex core boundary, which is where the peak swirl velocity is observed. For a magnification of 35 μm per pixel and a pulse separation time of 1 μs, this would mean that any estimated flow velocity that is smaller than 3.5 m/s is not reliable.

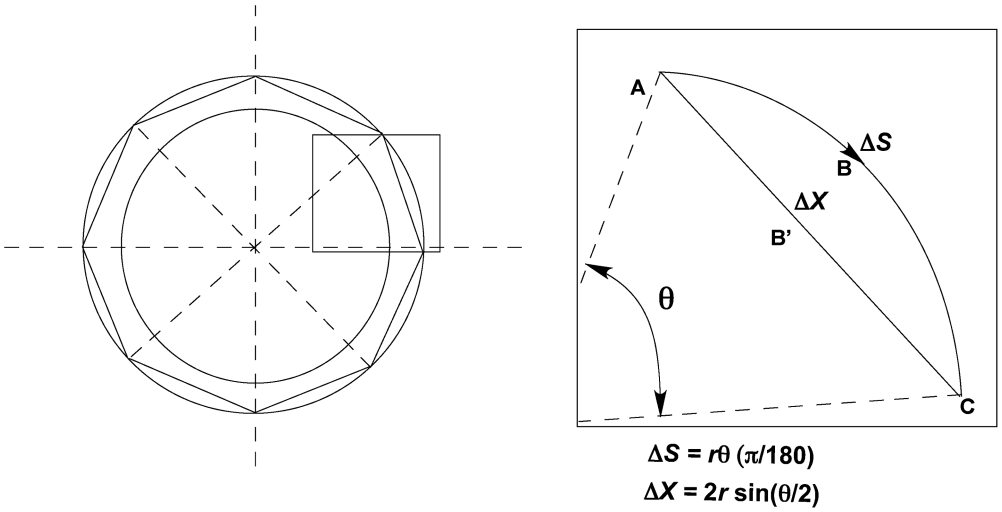

Fig. 13 Displacement estimation error from curvature effects.

This can also be defined as the precision of the measurement technique.

However, the upper bound for the pulse separation time is typically dictated by the correlation analysis software being used. For the correlation software used in the present study, the maximum window size cannot be larger than 128 pixels. To have relatively good correlation in the first iteration (before shifting the windows in successive iterations), the displacement of the particles should be less than one-fourth of the window size (i.e., 32 pixels or 1120 m/s). An increase in the pulse separation time (that eventually increases the particle displacement) reduces the measurement precision, while also reducing the maximum velocity that can be measured accurately.

F. Velocity Gradient Bias and Spatial Resolution

The effect of the velocity gradient on the mean velocity measurement is fundamentally different between LDV and PIV. On one hand, it is known that the average velocity measured within the interrogation volume for PIV will be biased toward the lower velocity. This is because of the higher number of low-velocity image pairs that contribute to the estimation of the correlation peak. LDV measurements, on the other hand, will be biased toward the higher velocities. This is because of the larger number of fast moving seed particles that pass through the measurement volume when compared with slower particles. It is known that the tip vortices have significantly high-velocity gradients inside their core boundary. As a result, any measurement technique that has a larger measurement volume will suffer from velocity gradient bias errors [41–43].

Chue [41] suggested that the measurement error in the mean velocity to be a function of the ratio of the spatial resolution of the instrument and the length scale of the shear layer. This ratio is given by the equation

$$\alpha = \frac{L_m}{r_c} \tag{28}$$

where L_m is the spatial resolution of the instrument and r_c is the length scale of the shear layer. Martin et al. [21] applied the theoretical method given by Kreid [42] to a self-similar vortex, and suggested the value of $\alpha \leq 0.1$ to resolve a high gradient flowfield accurately (with an uncertainty of less than 0.1%). This condition was estimated for a tip vortex trailing a subscale helicopter rotor, and cannot be applied for tip vortices that have different strengths. For example, tip vortices trailing from microscale rotors have very low-velocity gradients, while those of larger-scale rotors are very high. As a result, the value of this ratio can be larger for very small rotors while more stringent for larger-scale rotors.

It is known that larger windows that contain a larger number of seed particles are better for achieving statistical consistency in estimating the correlation signal. However, by plotting the uncertainty associated with the velocity gradient for two different window sizes (using the same normalized particle intensity), Raffel et al. [36] found that the smaller windows tolerate the velocity gradients better than the larger windows. The uncertainty was higher for the larger windows. This is because of the wider correlation peak that occurs when using larger windows, which is directly proportional to the local dynamic range. It was concluded that smaller windows are best suited for high-velocity gradient flows.

The interrogation window should be chosen such that the displacement gradient within the interrogation window (or its dynamic range) is not more than the size of the particle image. Any larger dynamic range will result in a larger correlation signal that introduces errors into the displacement estimates. This clearly suggests that the interrogation window should be chosen by taking into account the size of the particle images, as well as the velocity gradient in the flowfield. For a uniform grid (with constant distance between adjacent nodes throughout the region of focus) and a constant particle image size, the requirements become clear for high-velocity gradient flows, that is,

$$\Delta V_{i,i+1} \Delta t \leq d_\tau \tag{29}$$

where $\Delta V_{i,i+1}$ is the difference in velocity between adjacent nodes, d_τ is the particle image size, and Δt is the pulse separation time. This means that for a dynamic range of 35 m/s, as found in the rotor wake

Table 1 Pulse separation time and spatial resolution for various PIV measurements made in rotor wakes

Reference	C_T/σ_e	V_{norm}	V_{tip}, ms^{-1}	Core r_c/c	Chord, m	dV_θ/drc, s^{-1}	L_m/r_c	Δt, μs
Martin & Leishman [21]	0.087	0.17	89.28	0.15	0.045	2546	1.31	50
Van der Wall et al. [23]	0.057	0.25	218	0.05	0.121	3940	0.51	17
Richard & Raffel [44]	0.064	0.32	210	0.07	0.270	7526	0.47	10
McAlister [4]	0.095	0.40	87.2	0.051	0.104	6735	0.36	5
Ramasamy & Leishman [11]	0.083	0.305	27.1	0.165	0.019	2631	0.14	2
Martin & Leishman [3](LDV)	0.064	0.329	89.28	0.029	0.045	22553	0.03	——
Present experiments	0.064	0.33	89.28	0.032	0.045	21580	0.08	1

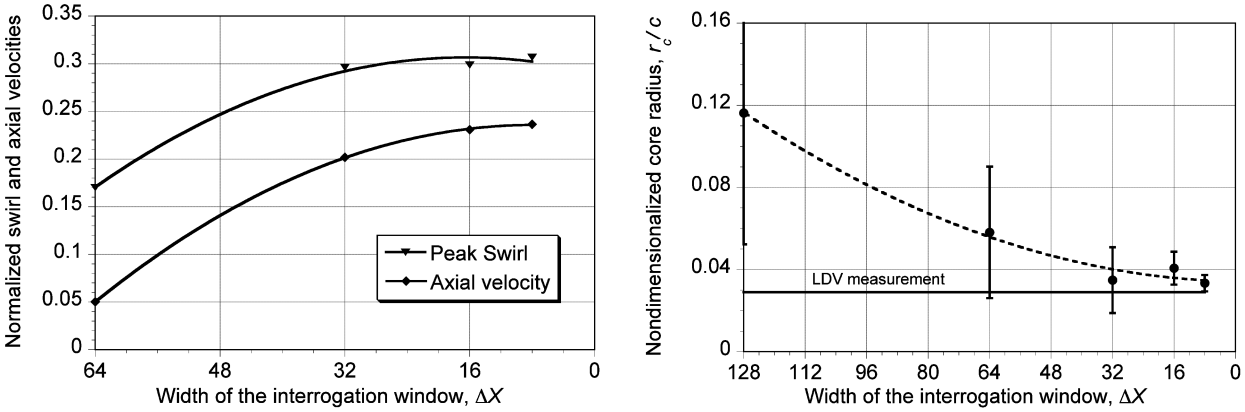

a) Swirl and axial velocity **b) Core size**

Fig. 14 Measured properties of the tip vortices at various resolutions.

flow examined in the present study (0 m/s at the vortex centers and 35 m/s at their core boundary), the maximum difference in velocity between adjacent nodes for a particle size of 4 μm at 1 μs is 4 m/s. This suggests that there should be at least nine points from the center of the vortex (its axis) to its core boundary to measure accurately the velocity gradients. The present measurements clearly have more than sufficient points. The absolute value of the velocity or displacement (mean value across the window) may not have any influence on the velocity estimation because the window shifting nature of the algorithm takes care of the mean flow value.

Table 1 gives an overview of the spatial resolution obtained in the present study when compared with other PIV measurements of rotor wakes and tip vortex flows. The importance of optimizing the interrogation window size in measuring accurately the velocity gradient is apparent from the last three sets of measurements. It can be seen that the PIV measurements made in the present study, with a spatial resolution similar to that of LDV ($\approx$80 μm), correlates well with the LDV measurements when determining the essential properties of a tip vortex. This includes core size, peak swirl velocity, and velocity gradient. In the work of [11], measurements were made on a very small rotor (suitable for a rotating-wing type of micro air vehicle) that was operated at low tip Reynolds numbers. As a result, the vortex core size was reported to be larger than that expected based on previously reported subscale measurements. This, in turn, resulted in lower measured velocity gradients, which is a result of the physics of the flow at this operating condition and not the shortcomings of the measurement technique.

Figures 14a and 14b show the measured peak swirl and axial velocities and the radius of the vortex core that are estimated using various interrogation windows of different sizes. Here, except for the window width, all other factors remain the same. It is apparent that both the velocities, as well as the normalized core radius, asymptote to constant values as the interrogation window reduces. An increase in window size increases the chances of having more correlation image pairs. However, for high-velocity gradient tip vortex flows, the correlation will be biased toward the lower velocity, as mentioned earlier. As a result, the estimated flow velocity values throughout the vortex are much lower when compared with their higher resolution counterparts. An interrogation window size of 8 pixels with 50% overlap ($L_m/r_c \approx 0.08$) seems to correlate well with the LDV measurements, suggesting that the current measurements of the rotor wake flow made with PIV are quantitatively reliable.

IX. Conclusions

An experiment has been conducted to identify and measure the sources of uncertainty associated with the application of PIV to the wake flow generated by a subscale helicopter rotor. Various critical factors have been found to have a significant influence on the estimation of the flow velocities in the high-velocity gradient, streamline curvature flows typical of those found inside rotor wakes and inside the blade tip vortices. The biggest sources of uncertainty lie in establishing the optimum laser pulse separation time and the interrogation window size. An inappropriate value of either of these quantities can completely change the magnitude and length scale of the measured flow structures.

The following are some specific conclusions that were obtained from this study:

1) PIV can be successfully employed for measuring the vortical flows and tip vortices trailing from rotor blades. Comparisons of the measured flow velocities between PIV and LDV were found in good agreement. The application of an iterative deformation grid increased the spatial resolution of PIV (120 μm) to that comparable to LDV (80 μm). As a result, the interrogation window size ($\geq$ 25 measurement velocity vectors inside the vortex core) is sufficient to resolve the steep velocity gradients present inside the blade tip vortices.

2) Calibration uncertainty reduces with an increase in the displacement of the seed particles. On one hand, this would mean that the swirl velocity measurements are more reliable near the vortex core boundary than nearer to the vortex axis (where the flow velocities are small). On the other hand, the axial velocity has its maximum value at the vortex core axis. However, the calibration procedure followed in this study was shown to be first order accurate in the axial flow direction.

3) Optimizing the laser pulse separation time is essential to reduce the errors associated with flow acceleration and curvature effects in PIV measurements of rotor wakes. Measurement errors in displacement estimation increase with an increase in laser pulse separation time for highly rotational flows such as blade tip vortices. The pulse separation time should be as small as possible; however, it should be chosen such that the particle displacement is sufficiently larger than the minimum measurable displacement.

4) The spatial resolution of the high-velocity gradient tip vortex flows that can be measured strongly depend on the particle image size (seed particle size). The local dynamic range between adjacent nodes should not be more than the particle image size, especially within the vortex core.

Acknowledgments

This research was supported by the Army Research Office (ARO) Grant W911NF0610394 and the Multi-University Research Initiative (MURI) under Grant W911NF0410176. Tom Doligalski is the technical monitor for both grants.

References

[1] Cook, C. V., "The Structure of the Rotor Blade Tip Vortex," Paper 3, Aerodynamics of Rotary Wings, AGARD CP-111, 13–15 Sept. 1972.

[2] Bagai, A., and Leishman, J. G., "Flow Visualization of Compressible Vortex Structures Using Density Gradient Techniques," *Experiments in Fluids*, Vol. 15, No. 6, Oct. 1993, pp. 431–442. doi:10.1007/BF00191786

[3] Martin, P. B., Pugliese, G., and Leishman, J. G., "High Resolution Trailing Vortex Measurements in the Wake of a Hovering Rotor," *Journal of the American Helicopter Society*, Vol. 49, No. 1, Jan. 2004, pp. 39–52.

[4] McAlister, K., "Rotor Wake Development During the First Revolution," *Journal of the American Helicopter Society*, Vol. 49, No. 4, Oct. 2004, pp. 371–390.

[5] Ramasamy, M., and Leishman, J. G., "Interdependence of Diffusion and Straining of Helicopter Blade Tip Vortices," *Journal of Aircraft*, Vol. 41, No. 5, Sept. 2004, pp. 1014–1024.

[6] Duraisamy, K., Ramasamy, M., Baeder, J., and Leishman, J. G., "Computational/Experimental Study of Hovering Rotor Tip Vortex Formation," *62nd Annual National Forum of the American Helicopter Society*, American Helicopter Society, Alexandria, VA, 7–9 May 2006.

[7] Heineck, J. T., Yamauchi, G. K., Wadcock, A. J., Lourenco, L., and Abergo, A. I., "Application of Three-Component PIV to a Hovering Rotor Wake," *56th Annual National Forum of the American Helicopter Society*, American Helicopter Society, Alexandria, VA, 2–4 May 2000.

[8] Yu., Y. H., and Tung, C., "The HART-II Test: Rotor Wakes and Aeroacoustics with Higher Harmonic Pitch Control (HHC) Inputs," *American Helicopter Society 58th Annual National Forum Proceedings*, American Helicopter Society, Alexandria, VA, 11–13 June 2002.

[9] Ramasamy, M., and Leishman, J. G., "A Generalized Model For Transitional Blade Tip Vortices," *Journal of the American Helicopter Society*, Vol. 51, No. 1, Jan. 2006, pp. 92–103.

[10] Boatwright, D. W., "Measurements of Velocity Components in the Wake of a Full-Scale Helicopter Rotor in Hover," USAAMRDL TR 72-33, 1972.

[11] Ramasamy, M., Leishman, J. G., and Lee, T. E., "Flow Field of a Rotating Wing MAV," *Journal of Aircraft*, Vol. 44, No. 4, July 2007, pp. 1236–1244.
doi:10.2514/1.26415

[12] Martin, P. B., Pugliese, G. J., and Leishman, J. G., "Laser Doppler Velocimetry Uncertainty Analysis For Rotor Blade Tip Vortex Measurements," *38th Aerospace Sciences Meeting and Exhibit*, CP 2000-0263, AIAA, Reston, VA, 10–13 Jan. 2000.

[13] Caradonna, F. X., and Tung, C., "Experimental and Analytical Studies of Model Helicopter Rotor in Hover," *Vertica*, Vol. 5, No. 2, 1981, pp. 149–161.

[14] Tung, C., Pucci, S. L., Caradonna, F. X., and Morse, H. A., "The Structure of Trailing Vortices Generated by Model Helicopter Rotor Blades," NASA TM 81316, 1981.

[15] Mahalingam, R., and Komerath, N. M., "Measurements of the Near Wake of a Rotor in Forward Flight," AIAA Paper 98-0692, 12–15 Jan. 1998.

[16] McAlister, K. W., "Measurements in the Near Wake of a Hovering Rotor," AIAA Paper 96-1958, 18–20 June 1996.

[17] Grant, I., Fu, S., Pan, X., and Wang, X., "The Application of an In-line, Stereoscopic, PIV System to 3-Component Velocity Measurements," *Experiments in Fluids*, Vol. 19, No. 3, July 1995, pp. 214–221.

[18] Lourenco, L., and Krothapalli, A., "On the Accuracy of Velocity and Vorticity Measurements with PIV," *Experiments in Fluids*, Vol. 18, No. 6, April 1995, pp. 421–428.
doi:10.1007/BF00208464

[19] Westerweel, J., "Fundamentals of Digital Particle Image Velocimetry," *Measurement Science and Technology*, Vol. 8, No. 12, Dec. 1997, pp. 1379–1392.
doi:10.1088/0957-0233/8/12/002

[20] Adrian, R. J., "Dynamic Ranges of Velocity and Spatial Resolution of Particle Image Velocimetry," *Measurement Science and Technology*, Vol. 8, No. 12, Dec. 1997, pp. 1393–1398.
doi:10.1088/0957-0233/8/12/003

[21] Martin, P. B., Leishman, J. G., Pugliese, J. P., and Anderson, S. L., "Stereoscopic PIV Measurements in the Wake of a Hovering Rotor," *56th Annual National Forum of the American Helicopter Society*, American Helicopter Society, Alexandria, VA, 2–4 May 2000.

[22] Wadcock, A. J., "Measurement of Vortex Strength and Core Diameter in the Wake of a Hovering Rotor," *AHS Technical Specialists' Meeting for Rotorcraft Acoustics and Aerodynamics*, American Helicopter Society, Alexandria, VA, 28–30 Oct. 1997.

[23] Van der Wall, B. G., and Richard, H., "Analysis Methodology for 3C-PIV Data of Rotary Wing Vortices," *Experiments in Fluids*, Vol. 40, No. 5, May 2006, pp. 798–812.
doi:10.1007/s00348-006-0117-x

[24] Ramasamy, M., Johnson, B., Huismann, T., and Leishman, J. G., "A New Method for Estimating Turbulent Vortex Flow Properties from Stereoscopic DPIV Measurements," *American Helicopter Society 63rd Annual National Forum Proceedings*, American Helicopter Society, Alexandria, VA, 1–3 May 2007.

[25] Leishman, J. G., "Seed Particle Dynamics in Tip Vortex Flows," *Journal of Aircraft*, Vol. 33, No. 4, 1996, pp. 823–825.

[26] Ramasamy, M., and Leishman, J. G., "Benchmarking PIV Measurements with LDV in the Wake of Hovering Rotor," AIAA Paper 2006-3479, 7–9 June 2006.

[27] Scarano, F., "Iterative Image Deformation Methods in PIV," *Measurement Science and Technology*, Vol. 13, No. 1, Jan. 2002, pp. R1–R19.
doi:10.1088/0957-0233/13/1/201

[28] Leishman, J. G., "Measurements of the Aperiodic Wake of a Hovering Rotor," *Experiments in Fluids*, Vol. 25, No. 4, Sept. 1998, pp. 352–361.
doi:10.1007/s003480050240

[29] Bjorkquist, D. C., "Stereoscopic PIV Calibration Verification," *11th International Symposium on Applications of Laser Techniques to Fluid Mechanics*, Instituto Superior Technico, Lisbon, Portugal, 8–11 July 2002.

[30] Keane, R. D., and Adrian, R. J., "Optimization of Particle Image Velocimeters. Part 1: Double Pulsed Systems," *Measurement Science and Technology*, Vol. 1, No. 11, Nov. 1990, pp. 1202–1215.
doi:10.1088/0957-0233/1/11/013

[31] Prasad, A., and Adrian, R., "Stereoscopic Particle Image Velocimetry Applied to Liquid Flows," *Experiments in Fluids*, Vol. 15, No. 1, June 1993, pp. 49–60.
doi:10.1007/BF00195595

[32] Adrian, R. J., "Particle Imaging Techniques for Experimental Fluid Mechanics," *Annual Review of Fluid Mechanics*, Vol. 23, 1991, pp. 261–304.

[33] Boillot, A., and Prasad, A. K., "Optimization Procedure for Pulse Separation in Cross-Correlation PIV," *Experiments in Fluids*, Vol. 21, No. 2, June 1996, pp. 87–93.
doi:10.1007/BF00193911

[34] Prasad, A. K., Adrian, R. J., Landreth, C. C., and Offutt, P. W., "Effect of Resolution on the Speed and Accuracy of Particle Image Velocimetry Interrogation," *Experiments in Fluids*, Vol. 13, Nos. 2–3, June 1992, pp. 105–116.
doi:10.1007/BF00218156

[35] Adrian, R. J., "Limiting Resolution of Particle Image Velocimetry for Turbulent Flow," *Advances in Turbulence Research*, Postech, Pohang, Korea, 27–29 March 1995.

[36] Raffel, M., Willert, C., and Kompenhans, J., *Particle Image Velocimtery: A Practical Guide*, 1st ed., Springer, Berlin, 1998.

[37] Christensen, K. T., "The Influence of Peak Locking Errors on Turbulence Statistics Computed from PIV Ensembles," *Experiments in Fluids*, Vol. 36, No. 3, March 2004, pp. 484–497.
doi:10.1007/s00348-003-0754-2

[38] Hocker, R., and Kompenhans, J., "Some Technical Improvements of Particle Image Velocimetry with Regard to its Application in Wind Tunnels," *International Congress on Instrumentation in Aerospace Simulation and Facilities*, IEEE, Piscataway, NJ, 18–21 Sept. 1989, pp. 545–554.

[39] Christensen, A., and Adrian, R. J., "Measurement of Instantaneous Acceleration Fields Using PIV," *Proceedings of the 4th International Symposium on Particle Image Velocimetry*, Gottingen, Germany, 17–19 Sept. 2001.

[40] Christensen, A., and Adrian, R. J., "Measurement of Instantaneous Eulerian Acceleration Field by Particle Image Velocimetry: Method and Accuracy," *Experiments in Fluids*, Vol. 33, No. 6, Dec. 2002, pp. 759–769.

[41] Chue, S. H., "Pressure Probes for Fluid Flow Measurements," *Progress in Aerospace Sciences*, Vol. 16, No. 2, 1975, pp. 147–223.
doi:10.1016/0376-0421(75)90014-7

[42] Kreid, D. K., "Laser-Doppler Velocimeter Measurements in Nonuniform Flow Field: Error Estimates," *Applied Optics*, Vol. 12, No. 8, 1974, pp. 1872–1881.

[43] Grant, I., "Particle Image Velocimetry: A Review," *Proceedings of the Institution of Mechanical Engineers Part C, Mechanical Engineering Science*, Vol. 211, 1997, pp. 55–76.
doi:10.1243/0954406971521665

[44] Richard, H., and Raffel, M., "Rotor Wake Measurements: Full Scale and Model Tests," *58th Annual National Forum of the American Helicopter Society*, American Helicopter Society, Alexandria, VA, 11–13 June 2002.

J. Gore
Associate Editor